Supporting Information

Photocatalytic Water Oxidation with a Prussian Blue Modified Brown TiO$_2$

Gulsum Gundogdu[a], Turkan Gamze Ulusoy Ghobadi[b], Sina Sadigh Akbari,[a] Ekmel Ozbay,[c,d,e] Ferdi Karadas[a,b*]

[a] Department of Chemistry, Faculty of Science, Bilkent University, 06800 Ankara, Turkey

[b] UNAM - National Nanotechnology Research Center, Institute of Materials Science and Nanotechnology, Bilkent University, 06800 Ankara, Turkey

[c] Department of Electrical and Electronics Engineering, Bilkent University, Ankara 06800, Turkey.

[d] NANOTAM – Nanotechnology Research Center, Bilkent University, Ankara 06800, Turkey

[e] Department of Physics, Bilkent University, Ankara 06800, Turkey.

[*]Corresponding author e-mail: karadas@fen.bilkent.edu.tr

1. Experimental Details

1.1. Chemicals and Reagents

All of the chemicals were used as received without further purification. Titanium (IV) butoxide (Ti(OBu)$_4$, 97%, Sigma–Aldrich), and Diethylene glycol (DEG), ethanol (EtOH) and diethyl ether (CH$_3$CH$_2$)$_2$O were also purchased from Sigma-Aldrich. Titanium(IV) oxide nanopowder (P25), Potassium hexacyanoferrate(III) (K$_3$Fe(CN)$_6$) and cobalt(II) nitrate hexahydrate (Co(NO$_3$)$_2$·6H$_2$O) were all purchased from Sigma-Aldrich. Na$_2$S$_2$O$_8$ aqueous buffer solutions were prepared adjusted to the desired pH by (0.1 M KH$_2$PO$_4$ and 0.1 M K$_2$HPO$_4$ diluted in deionized water with a pH close to 7). Millipore deionized water (resistivity: 18 MΩ cm^{-1}) was used in all of the experiments.

1.2. Synthesis of Black TiO$_2$ Nanoparticles, (b-TiO$_2$).

0.4 M Titanium(IV) butoxide (6.8 g) was mixed with 50 ml diethylene glycol (DEG) after stirring for 30 minutes at 1200 rpm yellow titanium glycolate gel is formed. 14.4 ml (8 molar times) of water was added and further stirred for 15 minutes. The hydrated titanium glycolate gel that has been formed was kept in a muffle furnace at 300°C for 2 hours. After leaving to cool at room temperature, the sample was washed using 100 ml each of ethanol, ether and water in order to remove impurities.

1.3. Synthesis of Prussian Blue coordinated TiO$_2$ and Black TiO$_2$ Nanoparticles, (PB/TiO$_2$ and PB/b-TiO$_2$).

An in situ synthetic method was adopted for the preparation of PB/TiO2 assemblies. Briefly, a Potassium hexacyanoferrate(III) solution (0.03 M) and TiO$_2$ powder solution (0.45 M) were dissolved in 15 mL water, afterwards magnetic stirred for 30 min at ambient temperature. Cobalt nitrate hexahydrate solution (0.04 M) dissolved in 15 mL water was added dropwise the resulting suspension was stirred for 12 hours. At last, the precipitate was centrifuged and washed with deionized water three times and the product was dried in oven at 60°C for 12 hours.

2. Characterization
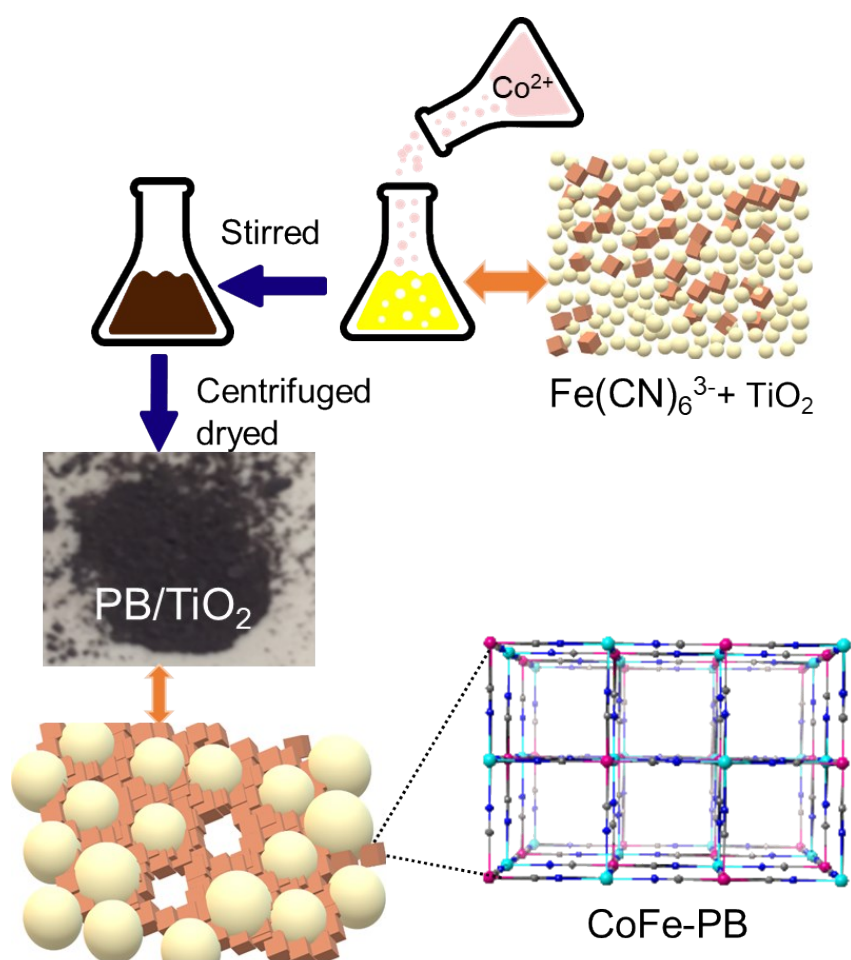
2.1. Photocatalytic O_2 Evolution Studies

Photocatalytic studies on nanoparticles have been performed using a suspension of powder sample with $Na_2S_2O_8$ as sacrificial agent/electron acceptor in a 0.1 M phosphate buffer, pH 7, at 25 ^oC under 1 sun illumination (100 mW.cm^{-2}). For each photocatalytic water oxidation test, 27 mg of catalysts with a mass ratio 1:1 of $Na_2S_2O_8$ dispersed in an 18 ml aqueous buffer solution placed in a round bottom flask. The reaction mixtures were purged before the test with N_2 in order to remove air. Photocatalytic O_2 evolution was conducted by GC (Agilent 7820A GC) equipped with a Molesieve column and a thermal conductivity detector (TCD). Argon gas was used as the carrier gas at a flow rate of 4 mL/min. 100 μL of the gas mixture was injected into the gas chromatograph by using Hamilton SampleLock syringe (1750SL, volume 0.5 mL, needle size 22 ga bevel tip, and needle L 51 mm). Oxygen evolution was monitored with each probe for 2 h illumination with the solar simulator (300 W Xe lamp, AM 1.5 global filter). A photocatalytic test was repeated several times to gain reliable results. A lower-bound TOF was determined by assuming that all cobalt ions in the bulk sample are catalytically active. The total amount of O_2 produced was calculated as the sum of the O_2 in the headspace (determined by GC) plus O_2 dissolved in the solvent (calculated using Henry's Law, with a constant of 769 atm^{-1}).
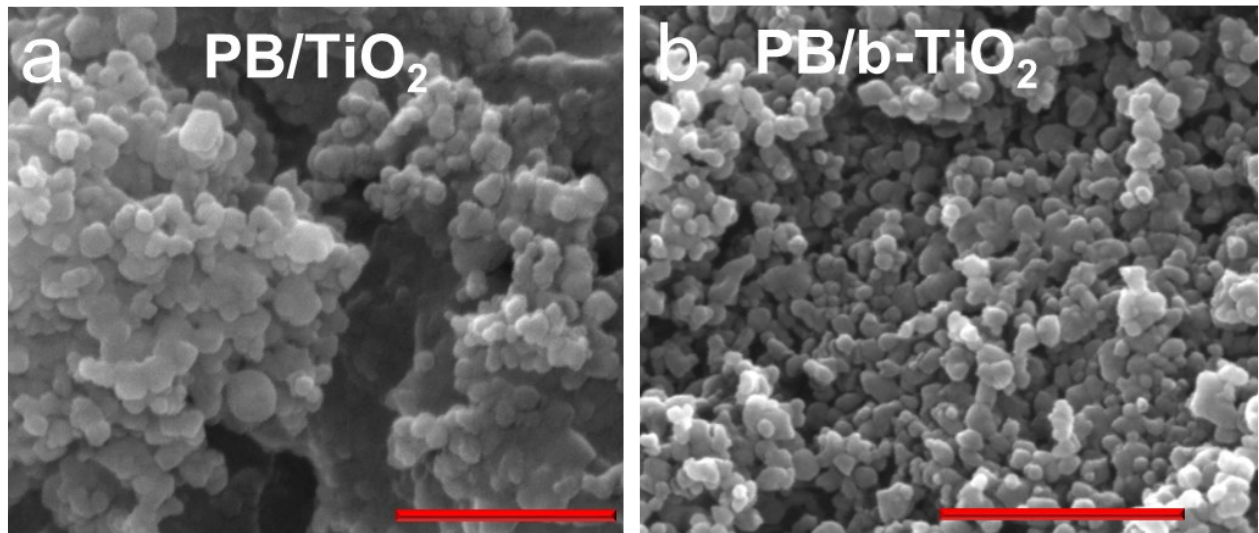
2.2. Materials Characterization

The morphological characteristics of the synthesized materials were performed using a scanning electron microscope (SEM, FEI – Quanta 200 FEG) and elemental composition using an energy dispersive X-ray detector (EDS) coupled to the SEM operated at 15 kV. A transmission electron microscope (TEM, Tecnai G2-F30, FEI) was operated at 300 kV. TEM samples were dispersed in ethanol and prepared on a holey carbon coated copper grid. The Powder X-ray diffraction (PXRD) patterns were collected by Panalytical X'pert Multi-Purpose using Bragg-Brentano geometry (Cu Kα radiation, λ = 0.15418 nm), in the range of 2θ from 15 to 70°. The IR spectra were measured using a Bruker ALPHA Platinum-ATR spectrometer in the wavenumber range 4.000–400 cm^{-1}. X-ray photoelectron spectroscopy (XPS, Thermo Scientific K-Alpha, Al K-Alpha radiation, hυ = 1486.6 eV) measurement was performed in survey mode by operating a flood gun to prevent surface charging with the pass energy and a step size set to 30 eV and 0.1 eV, respectively. Peak positions correction was calibrated by referencing the C1s peak position (284.8 eV) and shifting other peaks in the spectrum accordingly. For the optical characterization of the samples, reflectance diffusion spectra UV-Vis (UV/DRS) spectra of the powders were collected (via Cary 5000, Varian) in diffuse reflection

mode and converted to absorption spectra by Kubelka-Munk transformation. Photoluminescence (PL) measurements have been performed using Cary Eclipse. The fluorescence measurements of the samples were performed with excitation at a wavelength 300 nm b-TiO$_2$ and PB/b-TiO$_2$ and 325 nm TiO$_2$ and PB/TiO$_2$, recorded the emission profiles from 325 to 550 nm for b-TiO2 and PB/b-TiO2 and 350 to 550 nm for TiO$_2$ and PB/TiO$_2$.
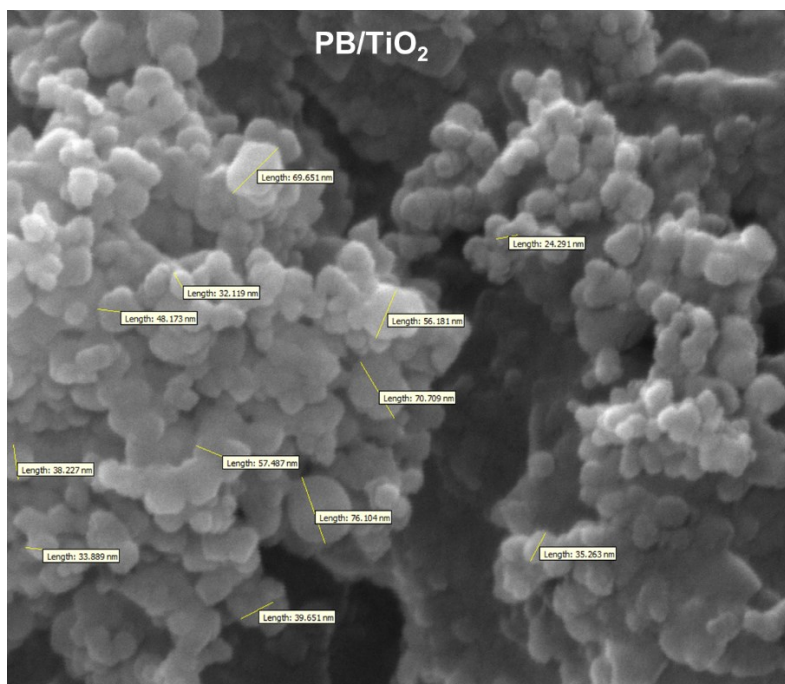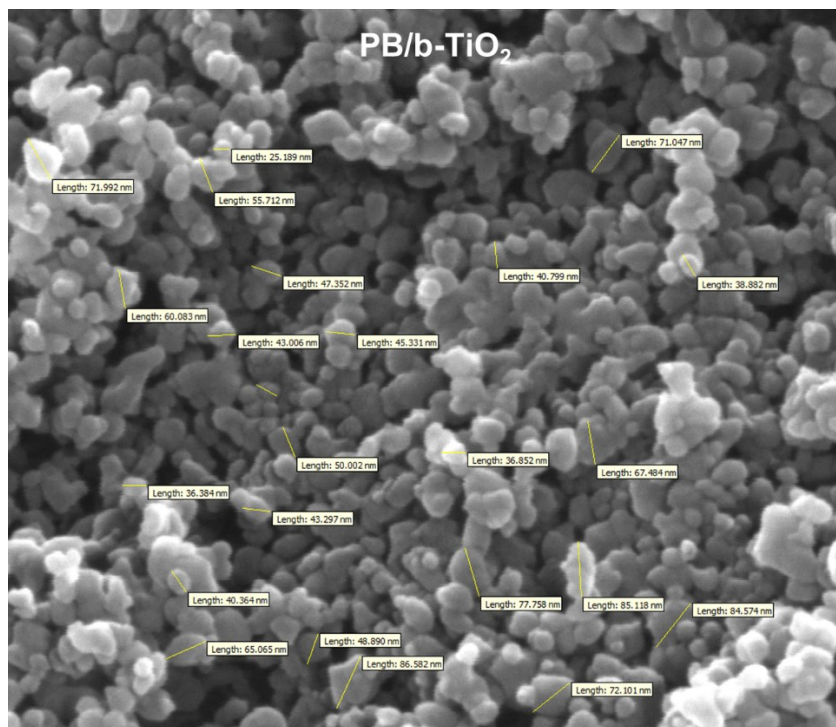
3. Supplementary Figures and Tables
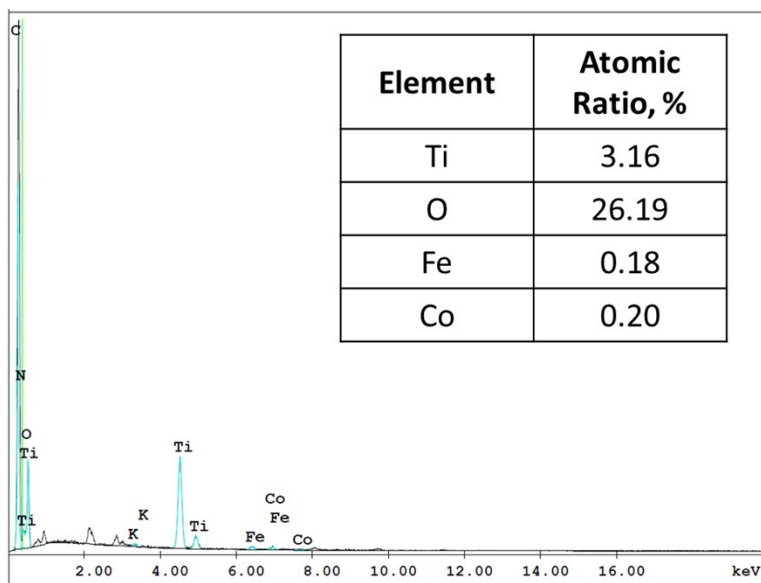

Fig. S1. Synthesis route for CoFe PB/TiO$_2$.

Fig. S2. SEM images for **(a)** PB/TiO$_2$ and **(b)** PB/b-TiO$_2$. Scale bars: 300 nm and 500 nm, respectively.
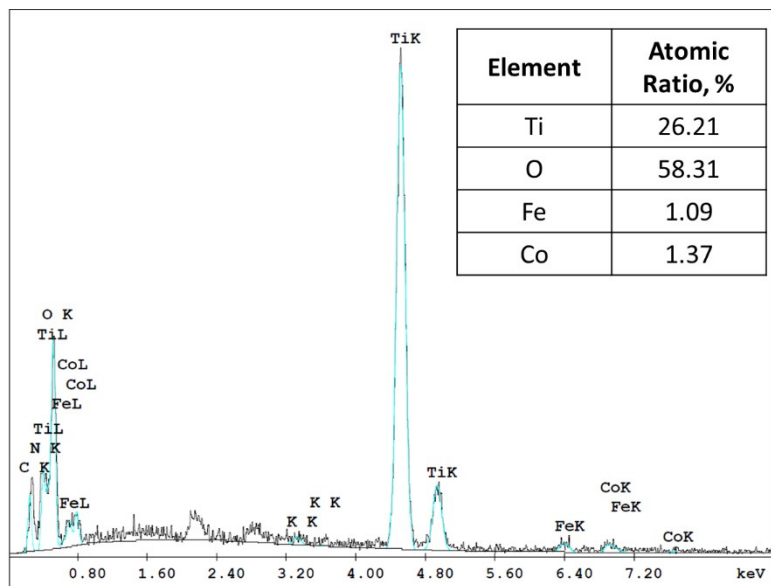

Fig. S3. SEM image of PB/TiO$_2$ NPs showing the average diameter varies from 24 to 73 nm. Scale bar: 300 nm.
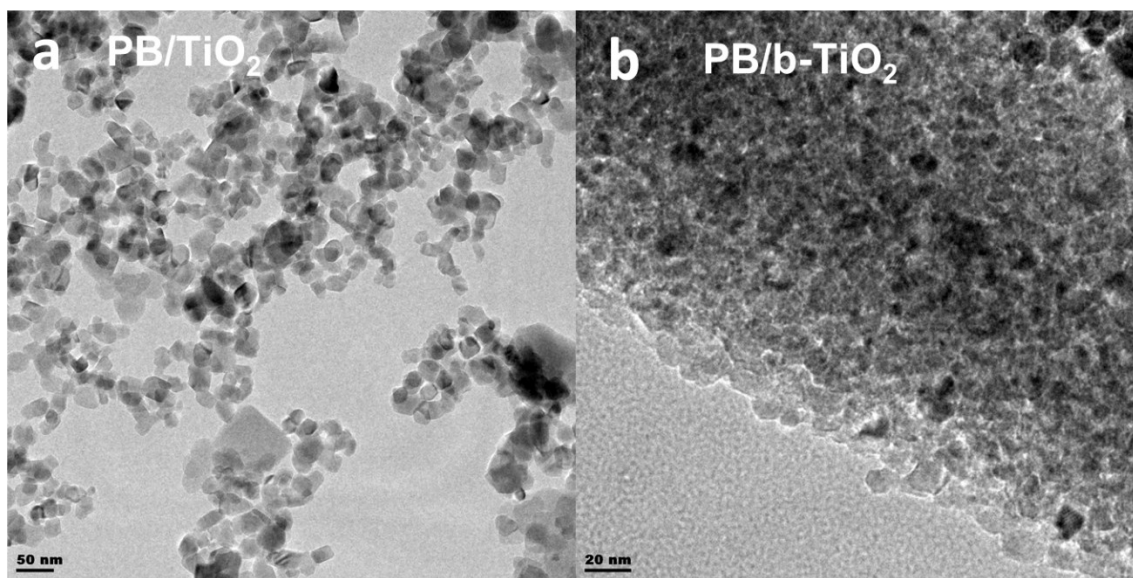
Fig. S4. SEM image of PB/b-TiO$_2$ NPs showing the average diameter varies from 25 to 87 nm. Scale bar: 500 nm.
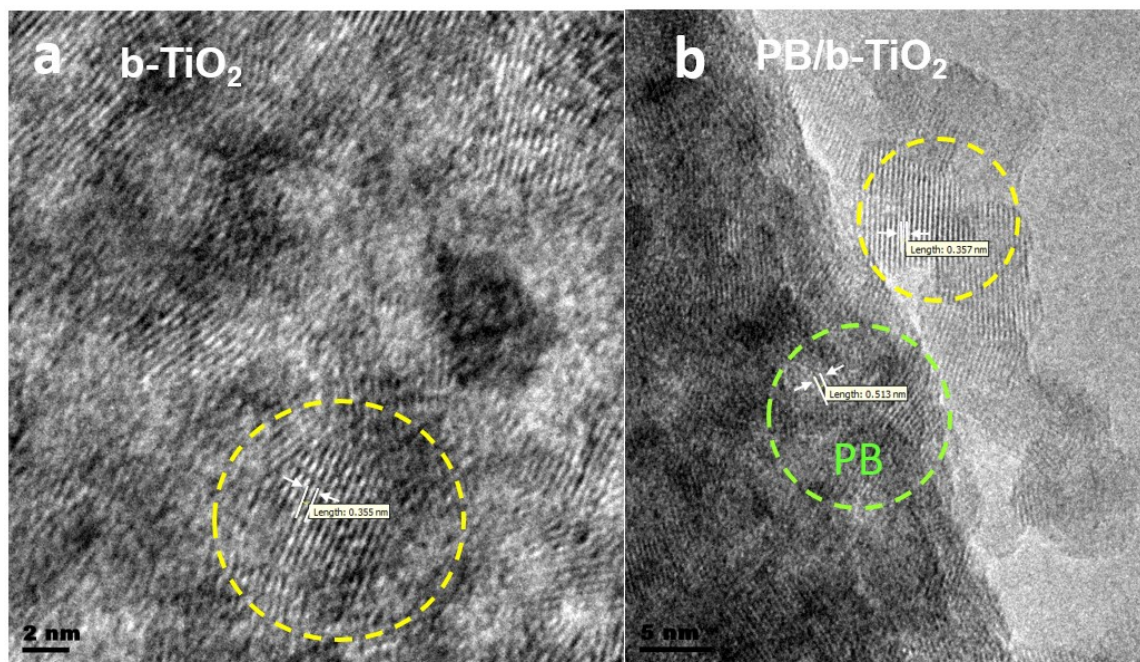

Element	Atomic Ratio, %
Ti	3.16
O	26.19
Fe	0.18
Co	0.20

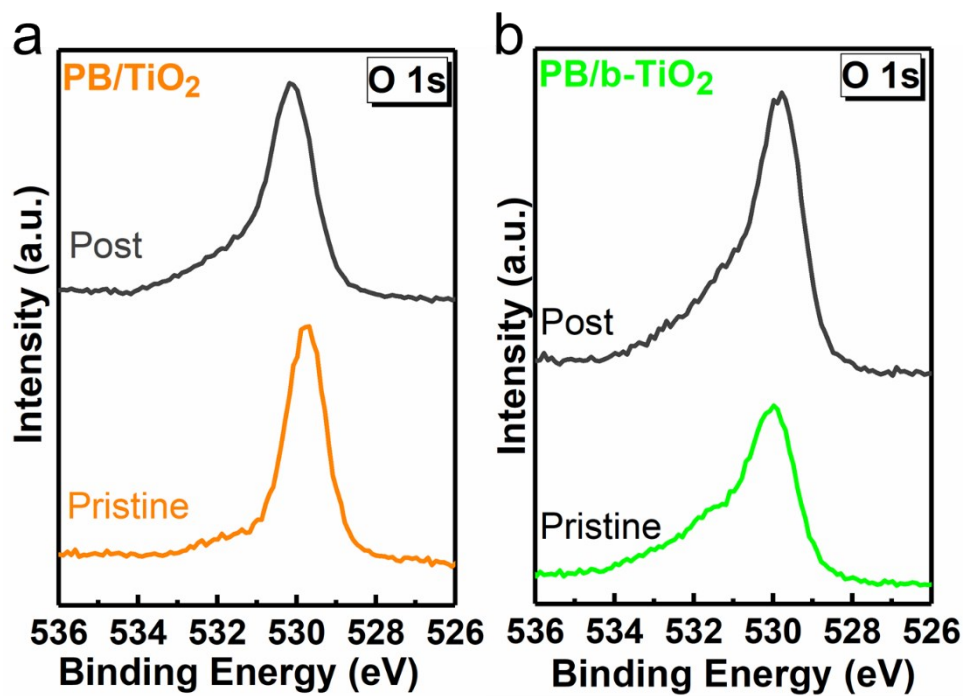**Fig. S5.** EDS analysis of PB/TiO$_2$.

Fig. S6. EDS analysis of PB/b-TiO$_2$.

Fig. S7. HR-TEM image of PB/TiO$_2$ and PB/b-TiO$_2$ Scale bar: 50 nm and 20 nm, respectively.

Fig. S8. HR-TEM images of a) b-TiO2 and b) PB/b-TiO$_2$ Scale bar: 2 nm and 5 nm, respectively. Anatase phase is highlighted by yellow and PB is highlighted by green color dashed circle.

Fig. S9. High resolution XPS spectra of O1s of the postcatalytic and pristine for PB/b-TiO$_2$ and PB/TiO$_2$ samples.
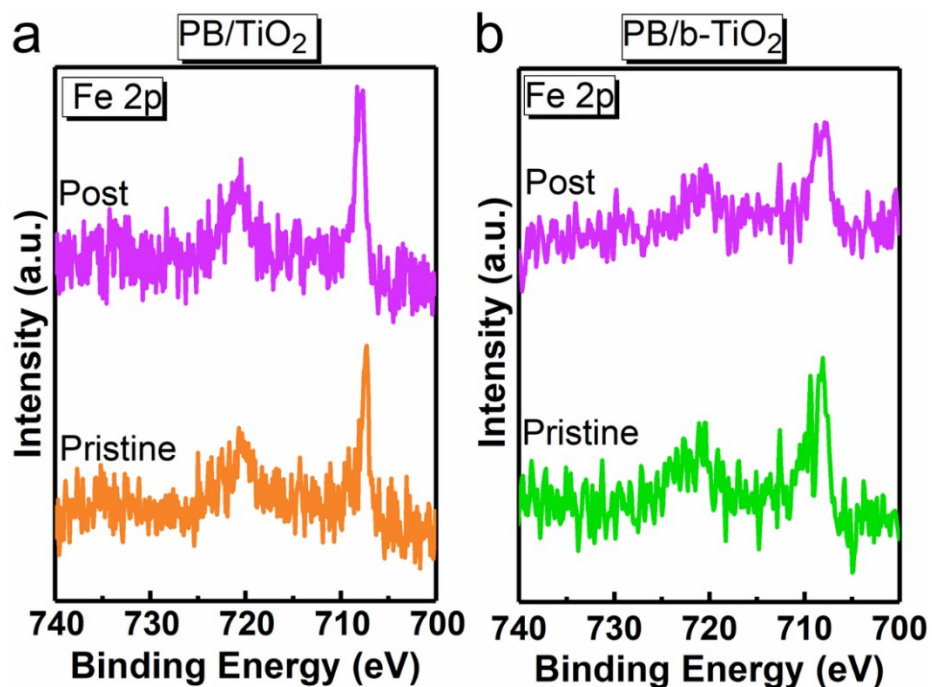
Fig. S10. High resolution XPS spectra of Fe2p for post catalytic PB/b-TiO$_2$ and pristine PB/TiO$_2$ samples.
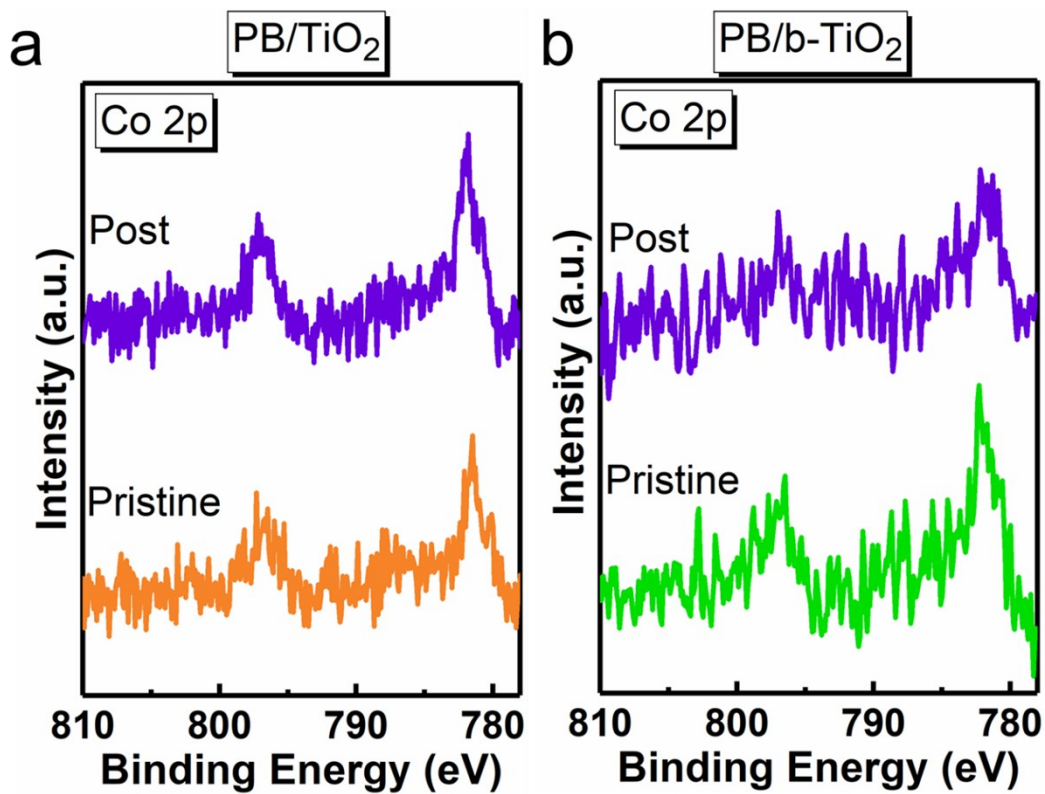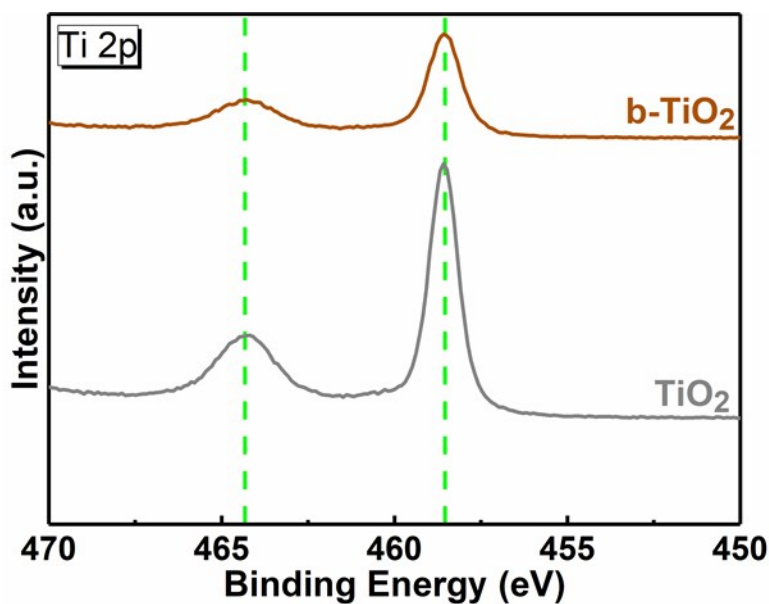

Fig. S11. XPS spectra of Co 2p for post catalytic PB/b-TiO$_2$ and pristine PB/TiO$_2$ samples.

Table S1. XPS Fe2p and Co2p regions obtained from pristine and post samples.

Compounds	Fe2p, eV				Co2p, eV			
	$2p_{3/2}$ Fe^{+2}	$2p_{1/2}$ Fe^{+2}	$2p_{3/2}$ Fe^{+3}	$2p_{1/2}$ Fe^{+3}	$2p_{3/2}$ Co^{+3}	$2p_{1/2}$ Co^{+3}	$2p_{3/2}$ Co^{+2}	$2p_{1/2}$ Co^{+2}
PB/TiO$_2$	707.3	721	709.5	-	-	-	781.5	796.7
Post	708	721	-	-	-	-	782	797
PB/b-TiO$_2$	708	721	710	723	-	-	782.4	797.5
Post	708	721	-	-	-	-	782	797

Table S2. Binding energies (eV) of O 1s XPS peaks for pristine and post-catalytic samples.

Compounds	O1s, eV	
	Pristine	Post
TiO$_2$ (P25)	529.8	-
PB/TiO$_2$	529.9	530
b-TiO$_2$	529.8	-
PB/b-TiO$_2$	530.7	529.8

Fig. S12. High resolution XPS spectra of Ti2p for TiO$_2$ samples.

Table S3. Binding energies (eV) of Ti 2p XPS peaks for P25 and obtained samples.
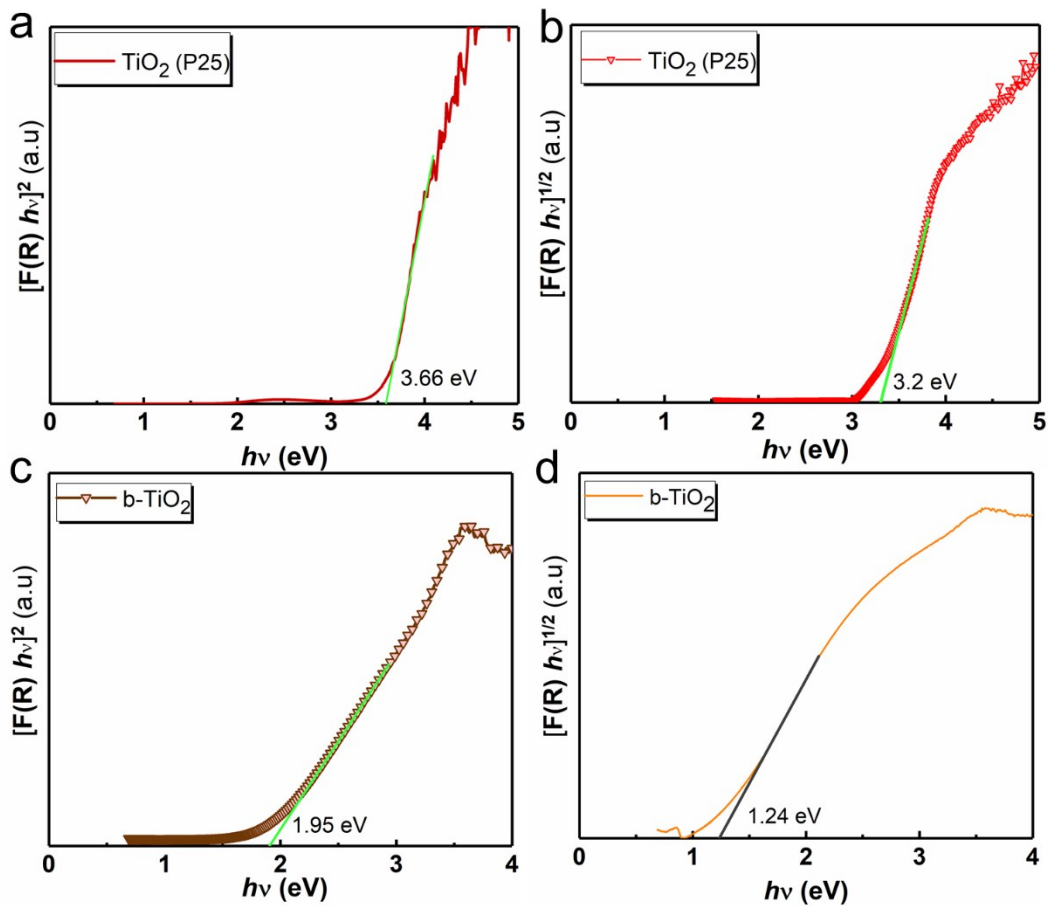
Compounds	Ti2p, eV	
	$2p_{3/2}$ Ti^{+4}	$2p_{1/2}$ Ti^{+4}
TiO$_2$ (P25)	458.6	464.3
PB/TiO$_2$	458.6	464.4
b-TiO$_2$	458.6	464.3
PB/b-TiO$_2$	459.3	465

The band gap energy is usually determined from diffuse reflectance spectra. The measured reflectance spectra can be transformed to the corresponding absorption spectra by applying the Kubelka–Munk function. The n factor $\left(F\left(R_\infty\right).h\vartheta\right)^n$ depends on the nature of the electron transition and is equal to 1/2 or 2 for the indirect and direct transition band gaps, respectively.[1]

$$\left(F\left(R_\infty\right).h\vartheta\right)^n = B\left(h\vartheta - E_g\right) \quad eq\ (1)$$

Through this transformation, the extrapolation with a linear function to zero absorption, the point at which the tangent line meets the x-axis equates to the band gap, Eg, value. Using the Tauc plots, the linearity of the plots against hv using n = 2 (direct) or n = 1/2 (indirect) are evaluated to assess the mode of transitions.

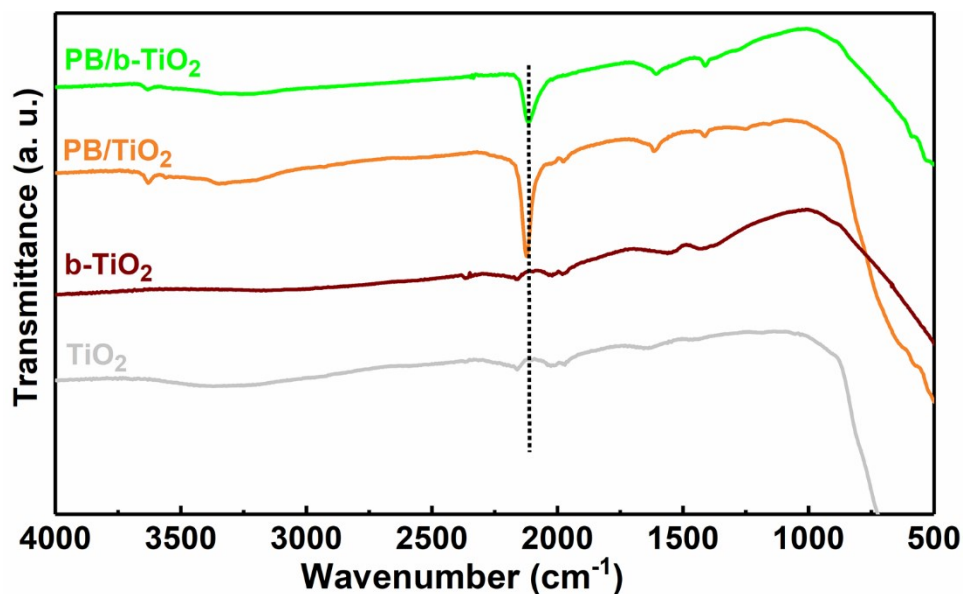In the case of TiO$_2$, the direct and indirect band gaps were found to be 3.66 eV and 3.2 eV, respectively. These values for b-TiO$_2$ were 1.95 eV and 1.24 eV (see below **Fig. S13**). For TiO$_2$, the direct transition shows unrealistic bandgap value reaching 3.66 eV, thus indirect transition is preferred. Likewise, for the synthesized b-TiO$_2$ (noting that it is not derived from P25, titanium butoxide is the starting material), the indirect transition shows 1.24 eV band gap, which may be expected for defective TiO$_2$ phase, however we use direct type transition fits for b-TiO$_2$ showing the band gap values 1.95 eV as can be seen in below figure. This is due to the results obtained from the band alignment by XPS analysis. As an independent (from optical absorption analysis) characterization, XPS based band alignment calculations show a band gap value of 1.92 eV, which is quite similar to direct band gap value. That's why, we used direct transition for b-TiO$_2$. It should also be noted that a band gap of 1.24 eV or 1.95 eV for b-TiO$_2$ does not change the conclusions drawn in this manuscript as both are well below the band gap of Degussa, which makes it a visible light harvesting semiconductor. The calculated band gaps are 3.2 and 1.95 eV for Degussa-P25 and b-TiO$_2$. A band gap study showed that the band gap of the b-TiO$_2$ was significantly lower (E$_g$= 1.95 eV) compared to the unmodified white Degussa TiO$_2$ (Eg= 3.20 eV).
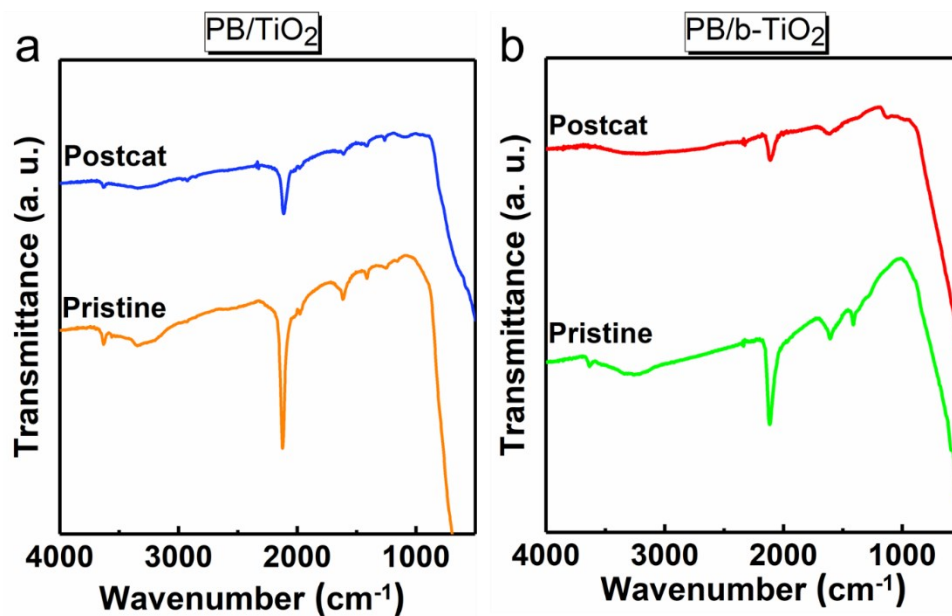
Fig. S13. The Kubelka-Munk absorption curves for **(a,c)** a direct allowed transitions (n=2) and **(b,d)** an indirect allowed transitions (n=1/2) for TiO_2 and b-TiO_2, respectively. The reflectance spectrums transformed according to eq 1. and plotted against the photon energy. The linear part of the plot is extrapolated to the x-axis.

Table S4. Comparison table between the PB/TiO$_2$ samples in this work and previously reported the most similar studies photocatalysts for water oxidation.
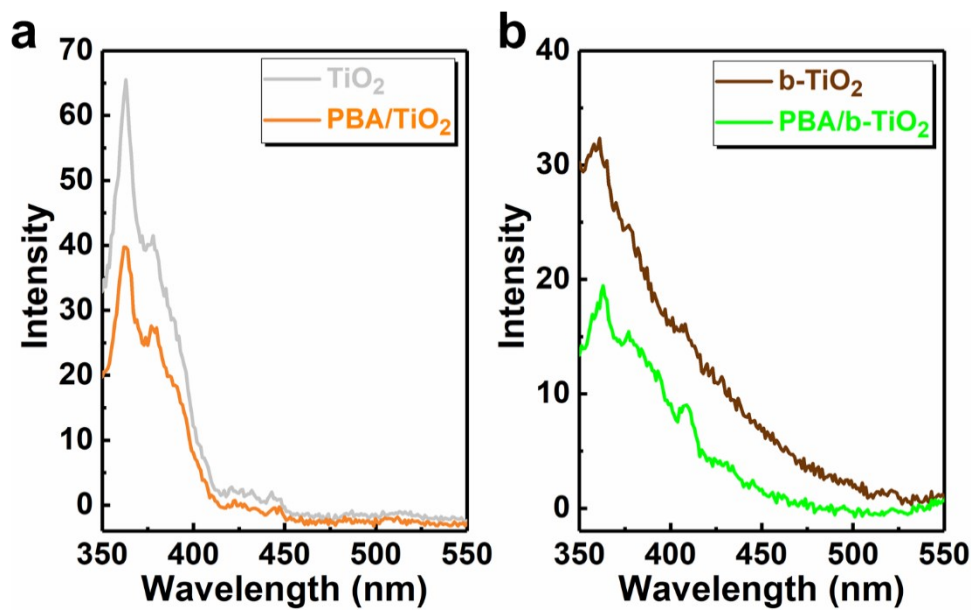
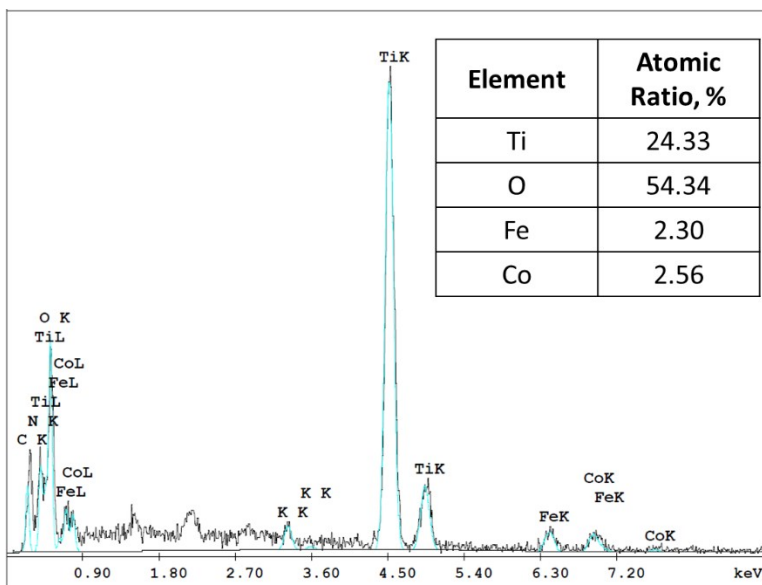| Photocatalyst	Light Source	λ (nm)	Amount of catalyst	Scavenger	pH	O$_2$ Evolved (µmol.h^{-1})	Ref
n-TiO$_2$	125 W Hg lamp	> 300	10 mg	H$_2$SO$_4$	acidic	80	[2]
TiO$_2$-ST01 Anatase TiO$_2$-TTO55N Rutile	500 W Xe lamp	≥ 330	8 g/L	Ce^{4+}	2-4	97.5 (anatase) 111.1 (rutile)	[3]
RuPy2@TiO2 RuPy6@TiO2	Blue LED light	470	100 µM	Na$_2$S$_2$O$_8$	7.2	2.78 0.693	[4]
cobalt-modified R-TiO2	300 W Xe lamp	> 500	100 mg	AgNO$_3$	8.0–8.5	2.5	[5]
RuCP2@Pt-TiO$_2$ RuCP2–Zr–RuP6@Pt–TiO$_2$ RuCP$_2$-Zr-RuP$_4$-Zr-RuP6@Pt-TiO$_2$	Blue LED light	470	100 mM	Na$_2$S$_2$O$_8$	7.3	3.20 2.11 0.543	[6]
Co$_3$O$_4$-loaded TiO$_2$	300 W Xe lamp	> 500	100 mg	AgNO$_3$ and La$_2$O$_3$	8.0-8.5	4.2 10.3	[7]
FeO$_x$–TiO$_2$ CoO$_x$–TiO$_2$ NiOx–TiO2	LED lamp	365	10 mg	AgNO$_3$	7	34.3 31.4 19.9	[8]
Chromium-Doped Titanium Dioxide	450 W Xe lamp	> 415	25 mg	AgNO3	3	50 µL/h	[9]
TiO$_2$ b-TiO$_2$ PB/TiO$_2$ PB/b-TiO$_2$ PB2/b-TiO$_2$	300 W Xe lamp	> 250	27 mg	Na$_2$S$_2$O$_8$	7	2.4 4.8 6.5 35.6 26	This work

Fig. S14. ATR-FTIR spectra for b-TiO$_2$, TiO$_2$, PB/b-TiO$_2$, and PB/TiO$_2$ samples. A broad peak below 460 cm^{-1} is observed that corresponds to Ti-O-Ti stretching vibrations. PB/b-TiO$_2$, and PB/TiO$_2$ samples display a sharp band at 1600 cm^{-1} and a broad band at around 3300 cm^{-1}, which can be assigned the M–O–H stretching mode and the bending mode of H$_2$O, respectively. The band at 1390 cm^{-1} is attributed to the asymmetric stretching of the carbonate species.

Fig. S15. ATR-FTIR spectra for pristine and post catalytic forms of **(a)** PB/TiO$_2$ and **(b)** PB/b-TiO$_2$ samples.

Fig. S16. The PL spectra for **(a)** TiO_2, PBA/TiO_2 and **(b)** $b\text{-}TiO_2$, and $PBA/b\text{-}TiO_2$ solutions in ethanol with an excitation wavelength of 325 and 300 nm, respectively. (10^{-3} in EtOH solutions, 2 mm cuvette length).

Element	Atomic Ratio, %
Ti	24.33
O	54.34
Fe	2.30
Co	2.56

Fig. S17. EDS analysis of $PB2/b\text{-}TiO_2$.

REFERENCES

1   P. Makuła, M. Pacia and W. Macyk, *J. Phys. Chem. Lett.*, 2018, 9, 6814–6817.

2   W. Vonach and N. Getoff, Z. Naturforsch., 1981, **36a**, 876-879.

3   G. R. Bamwenda, T. Uesigi, Y. Abe, K. Sayama and H. Arakawa, *Appl. Catal. A Gen.*, 2001, **205**, 117–128.

4   H. Otsuka, A. Kobayashi, M. Yoshida and M. Kato, *J. Photochem. Photobiol. A Chem.*, 2019, **369**, 189–194.

5   K. Maeda, K. Ishimaki, M. Okazaki, T. Kanazawa, D. Lu, S. Nozawa, H. Kato and M. Kakihana, *ACS Appl. Mater. Interfaces*, 2017, **9**, 6114–6122.

6   S. Furugori, A. Kobayashi, A. Watanabe, M. Yoshida and M. Kato, *ACS Omega*, 2017, **2**, 3901–3912.

7   K. Ishimaki, T. Uchiyama, M. Okazaki, D. Lu, Y. Uchimoto and K. Maeda, *Bull. Chem. Soc. Jpn.*, 2018, **91**, 486–491.

8   J. S. Schubert, J. Popovic, G. M. Haselmann, S. P. Nandan, J. Wang, A. Giesriegl, A. S. Cherevan and D. Eder, *J. Mater. Chem. A*, 2019, **7**, 18568–18579.

9   E. Borgarello, J. Kiwi, M. Grätzel, E. Pelizzetti and M. Visca, *J. Am. Chem. Soc.*, 1982, **104**, 2996–3002.